Robust two-qubit gates in silicon double quantum dots with composite pulses and optimized exchange control

Rui Yu(余睿)[1], Haoxuan Chen(陈浩煊)[4], Chenyi He(贺琛艺)[1], Fang Gao(高放)[3], and Chengxian Zhang(张程贤)[1,2,*]

[1]School of Physical Science and Technology, Guangxi University, Nanning 530004, China
[2]International Quantum Academy, Shenzhen 518048, China
[3]School of Electrical Engineering, Guangxi University, Nanning 530004, China
[4]State Key Laboratory of Precision Spectroscopy, East China Normal University, Shanghai 200241, China

Robust two-qubit gates are essential for scalable silicon spin qubits, but their fidelities are limited by microwave-control imperfections and charge-noise-induced exchange fluctuations. We propose a practical scheme for robust controlled-Z (CZ) and controlled-NOT (CNOT) gates in a silicon double quantum dot. By applying a transverse microwave drive, the effective Hamiltonian can be decomposed into two driven subspaces. In the subspace mainly controlled by the microwave field, a Broadband 1 (BB1) composite pulse is used to suppress errors in the microwave amplitude. In the exchange-assisted subspace, the microwave phases and durations are kept fixed, while a few piecewise-constant exchange amplitudes are optimized by a GRAPE-like procedure. This design reduces the sensitivity to both microwave-amplitude and exchange-amplitude errors while keeping the control waveform simple and experimentally friendly. Numerical simulations show that the optimized CNOT gate reaches a fidelity above 99.99% under experimentally relevant noise strengths, and the CZ gate also maintains a fidelity above 99.9%. These results indicate that combining composite pulses with optimized exchange control provides an experimentally feasible route to robust two-qubit gates in silicon spin qubits.

Keywords: semiconductor quantum dots, silicon spin qubits, exchange control, decoherence

PACS: 03.67.Lx, 73.21.La, 75.30.Et, 03.65.Yz

1. Introduction

Semiconductor spin qubits in silicon are a promising platform for scalable quantum information processing because they combine long coherence times, electrical control, and compatibility with advanced semiconductor fabrication technologies [1–5]. In recent years, silicon spin qubits have developed rapidly, with important progress in two-qubit gates, programmable quantum processors, and multiqubit spin-qubit arrays [6–11]. In particular, two-qubit gates with fidelities above the fault-tolerance threshold have been demonstrated [12–14]. Recent experiments have also shown reproducible high-fidelity operation, control at elevated temperatures, and fabrication approaches compatible with industrial processes [15–22]. These advances make silicon spin qubits attractive candidates for large-scale quantum information processing.

Despite this progress, robust two-qubit gate operation remains challenging. In silicon double quantum dots, entangling gates are commonly implemented by combining microwave-driven spin rotations with an electrically controlled exchange interaction. This control mechanism naturally introduces two important sources of error. One is the error in the microwave amplitude, which leads to pulse-length errors in driven spin rotations. The other is the fluctuation of the exchange interaction, which is mainly caused by charge noise because the exchange coupling is sensitive to the electrostatic environment. These two errors affect the gate dynamics in different ways: microwave amplitude errors distort the driven rotation, while exchange fluctuations directly change the conditional evolution and the accumulated two-qubit phase [18,23–25]. Therefore, a useful two-qubit gate design should not only yield a high ideal fidelity, but also reduce the sensitivity to both microwave and exchange errors.

Composite pulses and numerical optimal control are two useful approaches for reducing control errors. Composite pulses, such as the Broadband 1 (BB1) sequence, can suppress pulse-length errors and have been widely used in quantum control [26–29]. However, such analytical constructions are most convenient when the dynamics is dominated by a single control field. For two-qubit spin gates in silicon, the relevant driven subspace usually depends on both the microwave amplitude and the exchange interaction, making it difficult to compensate different error sources analytically. Numerical optimal control methods, such as the Gradient Ascent Pulse Engineering (GRAPE) al-

*Corresponding author. E-mail: cxzhang@gxu.edu.cn

gorithm, can treat multichannel control problems, but the resulting waveforms may be complicated for direct experimental implementation [30–33]. It is therefore useful to combine the analytical robustness of composite pulses with the flexibility of numerical optimization, while keeping the control waveform simple and experimentally friendly.

In this work, we propose a robust two-qubit scheme for a silicon double quantum dot by combining BB1 composite pulses with optimized exchange control. After transforming the driven two-spin Hamiltonian into the rotating frame, the system can be approximately decomposed into two driven two-level subspaces, denoted by S_1 and S_2. In the S_1 subspace, the dynamics is mainly governed by the microwave drive, so the BB1 pulse can be used to suppress errors in the microwave amplitude. In the S_2 subspace, the dynamics depends on both the microwave amplitude and the exchange interaction. We therefore keep the microwave phases and durations fixed by the BB1 construction, and optimize only the exchange amplitudes that are constant within each pulse segment. Based on this framework, we construct both controlled-Z (CZ) and controlled-NOT (CNOT) gates. Numerical results show that the optimized gates are robust against experimentally relevant microwave and exchange errors, while the required control waveform remains simple and compatible with exchange control in silicon spin-qubit devices.

2. Model

As shown in Fig. 1, we consider two electron spins confined in a silicon double quantum dot [34], and the corresponding Hamiltonian (taking $\hbar = 1$) can be described using the Heisenberg model, i.e.,

$$H(t) = J(t)\left(\mathbf{S}_L \cdot \mathbf{S}_R - 1/4\right) + \mathbf{S}_L \cdot \mathbf{B}_L + \mathbf{S}_R \cdot \mathbf{B}_R. \quad (1)$$

Here, $J(t)$ denotes the Heisenberg exchange interaction between the left spin $\mathbf{S}_L$ and the right spin $\mathbf{S}_R$, which can be experimentally tuned by the gate voltages. The magnetic fields acting on the two dots are denoted as $\mathbf{B}_L = [0, B_{y,L}(t), B_{z,L}(t) + B_z^{\text{ext}}]^T$ and $\mathbf{B}_R = [0, B_{y,R}(t), B_{z,R}(t) + B_z^{\text{ext}}]^T$ (in energy units). Here, the homogeneous external magnetic field in the z direction is denoted as B_z^{ext}, while the local magnetic field is denoted as $B_{z,q}(t) = B_{z,q}^0 + B_{z,q}^1(t)$ $(q = L, R)$, which introduces an inhomogeneous field between the two dots.

In the computational basis $\{|\uparrow\uparrow\rangle, |\downarrow\uparrow\rangle, |\uparrow\downarrow\rangle, |\downarrow\downarrow\rangle\}$, the static Hamiltonian in the absence of an ac transverse drive is written as

$$H_{\text{sta}} = \begin{pmatrix} E_z + E_z^1 & 0 & 0 & 0 \\ 0 & \frac{1}{2}(-J + \Delta E_z + \Delta E_z^1) & \frac{J}{2} & 0 \\ 0 & \frac{J}{2} & \frac{1}{2}(-J - \Delta E_z - \Delta E_z^1) & 0 \\ 0 & 0 & 0 & -E_z - E_z^1 \end{pmatrix} \quad (2)$$

Here $E_z = B_z^{\text{ext}} + (B_{z,L}^0 + B_{z,R}^0)/2$ is the average Zeeman splitting, $\Delta E_z = B_{z,R}^0 - B_{z,L}^0$ is the Zeeman-splitting difference between the two quantum dots, $E_z^1 = (B_{z,R}^1 + B_{z,L}^1)/2$ is the average Zeeman shift, and $\Delta E_z^1 = B_{z,R}^1 - B_{z,L}^1$ is the differential Zeeman shift. The quantity $\Delta E_z + \Delta E_z^1 = B_{z,R} - B_{z,L}$ describes the magnetic field gradient across the two dots. The instantaneous eigenenergies of H_{sta} are

$$E(|\uparrow\uparrow\rangle) = E_z + E_z^1, \quad (3a)$$

$$E(|\widetilde{\downarrow\uparrow}\rangle) = \frac{1}{2}\left[-J + \sqrt{(\Delta E_z + \Delta E_z^1)^2 + J^2}\right], \quad (3b)$$

$$E(|\widetilde{\uparrow\downarrow}\rangle) = \frac{1}{2}\left[-J - \sqrt{(\Delta E_z + \Delta E_z^1)^2 + J^2}\right], \quad (3c)$$

$$E(|\downarrow\downarrow\rangle) = -E_z - E_z^1. \quad (3d)$$

The corresponding eigenstates are $\{|\uparrow\uparrow\rangle, |\widetilde{\downarrow\uparrow}\rangle, |\widetilde{\uparrow\downarrow}\rangle, |\downarrow\downarrow\rangle\}$, where the mixed eigenstates are

$$|\widetilde{\downarrow\uparrow}\rangle = \sin\alpha|\downarrow\uparrow\rangle + \cos\alpha|\uparrow\downarrow\rangle, \quad (4a)$$

$$|\widetilde{\uparrow\downarrow}\rangle = -\cos\alpha|\downarrow\uparrow\rangle + \sin\alpha|\uparrow\downarrow\rangle. \quad (4b)$$

The mixing coefficients are defined by

$$\sin\alpha = \frac{\eta + \beta}{\sqrt{(\eta+\beta)^2 + 1}}, \quad (5a)$$

$$\cos\alpha = \frac{1}{\sqrt{(\eta+\beta)^2 + 1}}, \quad (5b)$$

$$\eta = \frac{\Delta E_z + \Delta E_z^1}{J}, \quad (5c)$$

$$\beta = \frac{\sqrt{J^2 + (\Delta E_z + \Delta E_z^1)^2}}{J}. \quad (5d)$$

In the following, we focus on the experimentally relevant regime $J \ll \Delta E_z + \Delta E_z^1$ [34], namely, the Zeeman splitting is much larger than the exchange interaction. Under this condition, we have

$$\cos\alpha \approx 0, \quad (6a)$$

$$\sin\alpha \approx 1, \quad (6b)$$

$$\sqrt{J^2 + (\Delta E_z + \Delta E_z^1)^2} \approx \Delta E_z + \Delta E_z^1 + \frac{J^2}{2(\Delta E_z + \Delta E_z^1)}. \quad (6c)$$

In this way, the eigenstates of the Hamiltonian are approximately product states of the two spins, and the eigenstate basis is therefore equivalent to the computational basis.

To facilitate the development of the two-qubit gates, we introduce the transverse ac drive on the two

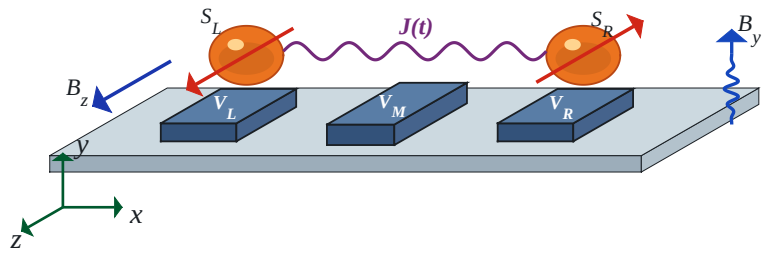


Fig. 1. Schematic of two spin qubits in a silicon double quantum dot. The left and right electron spins, denoted by S_L and S_R, are coupled through the tunable exchange interaction $J(t)$ controlled by the gate voltages. The two-dimensional electron gas of the device lies in the $x-z$ plane, and the static external field $B_z^{\rm ext}$ is applied along the in-plane z direction. The y direction is perpendicular to the device plane, and $B_y^{\rm ac}(t)$ represents the ac field generated by micromagnet-assisted EDSR. This control configuration enables the implementation of two-qubit gates.

spins with $B_{y,q}(t) = B_{y,q}^0 + B_{y,q}^1\cos(\omega t+\phi_0)$. Here, ω and ϕ denote the frequency and phase of the ac drive, respectively. Experimentally, the transverse ac drive can be generated using either electron spin resonance (ESR) [10] or electric dipole spin resonance (EDSR) [34] technologies. In this work, we consider using EDSR to generate an ac drive. We then transform the Hamiltonian into a rotating frame at angular frequency ω according to

$$H_{\rm rot}(t) = U_\omega H(t) U_\omega^\dagger - iU_\omega \dot{U}_\omega^\dagger, \tag{7}$$

where

$$U_\omega = \exp\left[i\omega t(S_{z,L}+S_{z,R})\right]. \tag{8}$$

After applying the rotating-wave approximation, the Hamiltonian is

$$H_{\rm rot}^{(1)} = \begin{pmatrix} E_z+E_z^1-\omega & -\frac{iB_{y,L}^1 e^{-i\phi_0}}{4} & -\frac{iB_{y,R}^1 e^{-i\phi_0}}{4} & 0 \\ \frac{iB_{y,L}^1 e^{i\phi_0}}{4} & \frac{1}{2}(-J+\Delta E_z+\Delta E_z^1) & \frac{J}{2} & -\frac{iB_{y,R}^1 e^{-i\phi_0}}{4} \\ \frac{iB_{y,R}^1 e^{i\phi_0}}{4} & \frac{J}{2} & \frac{1}{2}(-J-\Delta E_z-\Delta E_z^1) & -\frac{iB_{y,L}^1 e^{-i\phi_0}}{4} \\ 0 & \frac{iB_{y,R}^1 e^{i\phi_0}}{4} & \frac{iB_{y,L}^1 e^{i\phi_0}}{4} & -E_z-E_z^1+\omega \end{pmatrix} \tag{9}$$

It is useful to rewrite the Hamiltonian in the instantaneous eigenbasis of $H_{\rm sta}$ in the basis $\{|\uparrow\uparrow\rangle, |\widetilde{\downarrow\uparrow}\rangle, |\widetilde{\uparrow\downarrow}\rangle, |\downarrow\downarrow\rangle\}$. The driven Hamiltonian can be approximated as

$$H_{\rm rot}^{(2)} = \begin{pmatrix} E(|\uparrow\uparrow\rangle)-\omega & -\frac{iB_{y,L}^1 e^{-i\phi_0}}{4} & -\frac{iB_{y,R}^1 e^{-i\phi}}{4} & 0 \\ \frac{iB_{y,L}^1 e^{i\phi_0}}{4} & E(|\widetilde{\downarrow\uparrow}\rangle) & 0 & -\frac{iB_{y,R}^1 e^{-i\phi}}{4} \\ \frac{iB_{y,R}^1 e^{i\phi}}{4} & 0 & E(|\widetilde{\uparrow\downarrow}\rangle) & -\frac{iB_{y,L}^1 e^{-i\phi}}{4} \\ 0 & \frac{iB_{y,R}^1 e^{i\phi}}{4} & \frac{iB_{y,L}^1 e^{i\phi}}{4} & E(|\downarrow\downarrow\rangle)+\omega \end{pmatrix} \tag{10}$$

Note that the terms proportional to $B_{y,R}^1$ mainly induce off-resonant transitions and are further suppressed by the small mixing between the antiparallel spin states in the regime $J \ll \Delta E_z + \Delta E_z^1$. Experimentally, $B_{y,L}^1$ can be tuned from about 1 MHz to several MHz, while the magnetic-field gradient ΔE_z can be modulated from 100 MHz to 1 GHz. This large separation of energy scales justifies the approximations used above. Therefore, we also omit the $B_{y,R}^1$ relevant terms here [35]. Then, the Hamiltonian is decomposed into two blocks (subspaces) S_1 and S_2. The resonant driving frequency is chosen as

$$\omega = E_z + E_z^1 + \frac{1}{2}\left[J-\Delta E_z-\Delta E_z^1-\frac{J^2}{2(\Delta E_z+\Delta E_z^1)}\right], \tag{11}$$

which is the transition energy $E(|\uparrow\uparrow\rangle) - E(|\widetilde{\downarrow\uparrow}\rangle)$, and the block-diagonalized Hamiltonian as

$$H_{\rm rot}^{(3)} = C_1\widetilde{I} + C_2\widetilde{P} + \begin{pmatrix} 0 & \frac{B_{y,L}^1}{4}e^{-i\phi} & 0 & 0 \\ \frac{B_{y,L}^1}{4}e^{i\phi} & 0 & 0 & 0 \\ 0 & 0 & -\frac{J}{2} & \frac{B_{y,L}^1}{4}e^{-i\phi} \\ 0 & 0 & \frac{B_{y,L}^1}{4}e^{i\phi} & \frac{J}{2} \end{pmatrix} \tag{12}$$

Here, we have defined $\phi = \phi_0 + \pi/2$ for convenience, $\widetilde{I}$ denotes the identity operator and

$$\widetilde{P} = |\widetilde{\uparrow\downarrow}\rangle\langle\widetilde{\uparrow\downarrow}| + |\downarrow\downarrow\rangle\langle\downarrow\downarrow| \tag{13}$$

projects onto the S_2 block. The coefficients are

$$C_1 = \frac{1}{2}(\Delta E_z+\Delta E_z^1) + \frac{J^2}{4(\Delta E_z+\Delta E_z^1)} - \frac{J}{2}, \tag{14a}$$

$$C_2 = -(\Delta E_z+\Delta E_z^1) - \frac{J^2}{2(\Delta E_z+\Delta E_z^1)} + \frac{J}{2}. \tag{14b}$$

The term $C_1\widetilde{I}$ gives a global phase, while $C_2\widetilde{P}$ contributes a relative phase to the second subspace. We temporarily omit this relative phase during the pulse design and restore it later in the numerical calculation. The two subspace Hamiltonians are therefore

$$H_{S_1}^0 = \begin{pmatrix} 0 & \frac{h}{2}e^{-i\phi} \\ \frac{h}{2}e^{i\phi} & 0 \end{pmatrix}, \tag{15}$$

and

$$H_{S_2}^0 = \begin{pmatrix} -\frac{J}{2} & \frac{h}{2}e^{-i\phi} \\ \frac{h}{2}e^{i\phi} & \frac{J}{2} \end{pmatrix}. \tag{16}$$

For convenience, here we have set $B_{y,L}^1 = 2h$.

The S_1 block is controlled only by the transverse microwave field h. In contrast, the S_2 block is controlled jointly by h and the exchange interaction J.

Directly designing a robust pulse in S_2 is therefore more involved. To implement robust two-qubit gates in the whole space, we first construct a BB1 pulse sequence in S_1 to suppress microwave amplitude error, and then use the pulse durations fixed in S_1 by this construction to numerically optimize the exchange interaction as a piecewise pulse sequence in S_2.

3. Two-qubit entangling gates

3.1. Robust operations in S_1 subspace with BB1 pulses

In the S_1 subspace the Hamiltonian can be written as

$$H_{S_1} = \frac{h}{2}\left(\cos\phi\,\sigma_x + \sin\phi\,\sigma_y\right). \tag{17}$$

Here, the Pauli matrices are defined in the S_1 subspace with $\sigma_z = |\uparrow\uparrow\rangle\langle\uparrow\uparrow| - |\widetilde{\downarrow\uparrow}\rangle\langle\widetilde{\downarrow\uparrow}|$. The evolution operator for a single pulse of duration τ in S_1 is

$$\begin{aligned} U_{S_1}(\theta,\phi) &= \exp\left[-iH_{S_1}\tau\right] \\ &= \begin{pmatrix} \cos\dfrac{\theta}{2} & -ie^{-i\phi}\sin\dfrac{\theta}{2} \\ -ie^{i\phi}\sin\dfrac{\theta}{2} & \cos\dfrac{\theta}{2} \end{pmatrix}. \end{aligned} \tag{18}$$

Here, $U_{S_1}(\theta,\phi)$ represents a rotation angle $\theta = h\tau$ about an axis with azimuthal angle ϕ in the $x-y$ plane on the Bloch sphere. In this work, to shorten the gate time, we take h to be a square pulse. For a target rotation $U_{S_1}(\theta,\phi)$, the BB1 composite pulse is composed of four elementary rotations, namely, $U_{\rm BB1} = U(\theta_4,\phi_4)U(\theta_3,\phi_3)U(\theta_2,\phi_2)U(\theta_1,\phi_1)$. The rotation angles and phases of the four pulses are chosen as

$$\begin{aligned} &\theta_1 = \theta_3 = \pi, \qquad \phi_1 = \phi_3 = \phi + \arccos\left(-\frac{\theta}{4\pi}\right), \\ &\theta_2 = 2\pi, \qquad \phi_2 = 3\phi_1 - 2\phi, \\ &\theta_4 = \theta, \qquad \phi_4 = \phi. \end{aligned} \tag{19}$$

For the construction of a CZ gate, the desired operation is the identity in S_1 and a $Z(\pi)$ rotation in S_2. We then choose $\theta = 2\pi$ and $\phi = 0$. On the other hand, for the construction of a CNOT gate, the desired operation in S_1 is a NOT gate and the identity in S_2. Here the CNOT gate is defined with the right qubit as the control qubit and the left qubit as the target qubit, since the working basis $\{|\uparrow\uparrow\rangle, |\widetilde{\downarrow\uparrow}\rangle, |\widetilde{\uparrow\downarrow}\rangle, |\downarrow\downarrow\rangle\}$ is ordered differently from the standard computational basis [35]. This can be implemented by choosing $\theta = \pi$ and $\phi = 0$. Fig. 2 presents the fidelity of the identity operation using the BB1 pulse in the S_1 subspace. The fidelity remains nearly unity throughout the range considered, demonstrating that the BB1 sequence strongly suppresses microwave amplitude error in the microwave drive. Since the $\mathcal{S}_1$ and S_2 blocks are driven by the same microwave sequence, the BB1 pulse also fixes the segment durations and phases used in the S_2 block, where only the exchange amplitudes are further optimized.

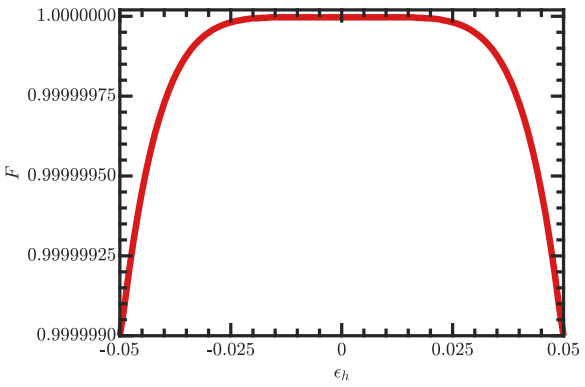


Fig. 2. Fidelity robustness of the identity operation using the BB1 pulse in the S_1 subspace under microwave amplitude error ϵ_h. The fidelity remains nearly unity over the error range considered, demonstrating the strong robustness of the BB1 construction against microwave amplitude error.

3.2. CZ gate

For the BB1 rotation above, the duration of each segment is

$$\tau_1 = \tau_3 = \frac{\pi}{h}, \quad \tau_2 = \frac{2\pi}{h}, \quad \tau_4 = \frac{2\pi}{h}. \tag{20}$$

After the BB1 construction in the S_1 block, these four pulse durations $\{\tau_k\}_{k=1}^4$ are fixed. These durations must be used simultaneously in the S_2 block, because the two blocks originate from the same block-diagonal Hamiltonian and are driven by the same microwave pulse sequence. Therefore, the microwave control field h cannot be optimized independently in the S_2 block. Instead, for each fixed BB1 pulse segment, we optimize the corresponding exchange interaction J_k. The resulting control sequence in the S_2 block is described by

$$U_{S_2}(\mathbf{J}) = U_{S_2}^{(4)}(J_4,\tau_4)U_{S_2}^{(3)}(J_3,\tau_3)U_{S_2}^{(2)}(J_2,\tau_2)U_{S_2}^{(1)}(J_1,\tau_1), \tag{21}$$

where $\mathbf{J} = (J_1, J_2, J_3, J_4)$ and

$$U_{S_2}^{(k)}(J_k,\tau_k) = \exp\left[-iH_{S_2}^{(k)}(J_k,h_k,\phi_k)\tau_k\right]. \tag{22}$$

Here h_k and ϕ_k are fixed by the BB1 pulse in the S_1 block, whereas J_k is treated as the tunable control parameter in the S_2 block. For simplicity, we keep $h_k \equiv h$ unchanged throughout this work. Note that since the

exchange interaction is designed as a piecewise pulse, the resonant driving frequency is also chosen segment by segment. For the kth pulse segment with nominal exchange amplitude J_k, we use

$$\omega_k = E_z + E_z^1 + \frac{1}{2}\left[J_k - \Delta E_z - \Delta E_z^1 - \frac{J_k^2}{2(\Delta E_z + \Delta E_z^1)}\right]. \tag{23}$$

Thus, the microwave drive is implemented as a piecewise frequency modulated microwave field, with $\omega(t) = \omega_k$ for $t_{k-1} \le t < t_k$. This choice keeps each segment resonant with the corresponding transition defined by the nominal exchange amplitude.

Inserting the BB1 phases and pulse durations gives

$$U_{S_2}^{(k)} = \begin{pmatrix} \cos\frac{\Omega_k\tau_k}{2} + i\frac{J_k}{\Omega_k}\sin\frac{\Omega_k\tau_k}{2} & -ie^{-i\phi_k}\frac{h}{\Omega_k}\sin\frac{\Omega_k\tau_k}{2} \\ -ie^{i\phi_k}\frac{h}{\Omega_k}\sin\frac{\Omega_k\tau_k}{2} & \cos\frac{\Omega_k\tau_k}{2} - i\frac{J_k}{\Omega_k}\sin\frac{\Omega_k\tau_k}{2} \end{pmatrix} \tag{24}$$

where $\Omega_k = \sqrt{h^2 + J_k^2}$. The target total operator in the S_2 block is

$$U_{S_2} = U_{S_2}^{(4)} U_{S_2}^{(3)} U_{S_2}^{(2)} U_{S_2}^{(1)}$$

which is expected to be a $Z(\pi)$ rotation. Together with an identity operation, up to a global phase, in the S_1 block, this realizes the desired CZ gate in the original two-qubit computational basis. Then, the remaining question is how to determine $\mathbf{J}$ to obtain robust operations.

In realistic silicon double quantum dots, the dominant noise source during entangling operations is typically the fluctuation of the exchange interaction induced by charge noise. Meanwhile, imperfect microwave control gives rise to additional fluctuations in the drive amplitude h. In this work, we assume both errors to be quasistatic because they vary on a much longer time scale than the gate operation time [36]. To include the effect of quasistatic errors, the control parameters become

$$h_k \to h_k(1+\epsilon_h), \qquad J_k \to J_k(1+\epsilon_J). \tag{25}$$

Here, ϵ_h describes the error term in h, while ϵ_J describes the error term in J, which are denoted as microwave amplitude error and exchange amplitude error, respectively.

In contrast to the S_1 block, where the BB1 sequence provides an analytic suppression of microwave amplitude error, the S_2 block is governed by both the microwave drive associated with h and the exchange interaction J. In this case, fluctuations in J, mainly induced by charge noise, are coupled to the driven dynamics, while imperfect microwave control introduces additional errors in h. As a result, deriving a closed-form composite pulse sequence that simultaneously compensates for both error channels is generally intractable. We therefore numerically determine $\mathbf{J}$ using a GRAPE-like algorithm.

For a given noise realization $\boldsymbol{\epsilon} = (\epsilon_h, \epsilon_J)$, the noisy evolution operator is denoted by $U_{S_2}(\mathbf{J};\boldsymbol{\epsilon})$. In the algorithm, we calculate the fidelity as

$$F_{S_2}^c(\mathbf{J};\boldsymbol{\epsilon}) = \left|\mathrm{Tr}\left[U_{\mathrm{tar},S_2}^\dagger U_{S_2}(\mathbf{J};\boldsymbol{\epsilon})\right]\right|^2/4. \tag{26}$$

Here $F_{S_2}^c$ denotes the normalized Hilbert-Schmidt fidelity in the two-dimensional subspace. The cost function is then defined as the noise-averaged infidelity

$$\mathcal{C}(\mathbf{J}) = 1 - \sum_{\mu=1}^{N_s} w_\mu F_{S_2}^c\left(\mathbf{J};\boldsymbol{\epsilon}_\mu\right), \qquad \sum_{\mu=1}^{N_s} w_\mu = 1, \tag{27}$$

where $\{\boldsymbol{\epsilon}_\mu\}$ is a set of sampled noise values, N_s is the number of sampled noise points, and w_μ are the corresponding weights. We first optimize a four-segment exchange pulse, where the four segment durations are fixed by the BB1 sequence in the S_1 subspace. The optimization procedure is summarized as follows.

1. Fix the BB1 pulse angles and phases in the S_1 block. This step determines the four operation durations $\{\tau_k\}_{k=1}^4$, as shown in Eq. (20).

2. Use the same durations $\{\tau_k\}_{k=1}^4$ in the S_2 block and initialize the exchange interactions $\mathbf{J}^{(0)} = (J_1^{(0)}, J_2^{(0)}, J_3^{(0)}, J_4^{(0)})$ within the experimentally allowed range, and ensure that $J \ll \Delta E_z + \Delta E_z^1$.

3. For each trial control vector $\mathbf{J}$ and each noise realization $\boldsymbol{\epsilon}_\mu$, calculate the four segment propagators $U_{S_2}^{(k)}$ and construct the total operator $U_{S_2}(\mathbf{J};\boldsymbol{\epsilon}_\mu)$.

4. Evaluate the robust cost function $\mathcal{C}(\mathbf{J})$ defined in Eq. (27).

5. Update the exchange interaction value $\mathbf{J}$ to reduce $\mathcal{C}(\mathbf{J})$. In a GRAPE-like implementation, this update can be performed by calculating the sensitivity of the fidelity to each exchange interaction J_k using forward and backward propagators. The derivative of a segment operator is

$$\frac{\partial U_{S_2}^{(k)}}{\partial J_k} = -i\int_0^{\tau_k} e^{-iH_k(\tau_k - t)}\frac{\partial H_k}{\partial J_k}e^{-iH_k t}\,dt, \tag{28}$$

where $H_k \equiv H_{S_2}^{(k)}(J_k, h_k, \phi_k)$. This expression gives the local gradient of the objective function with respect to J_k.

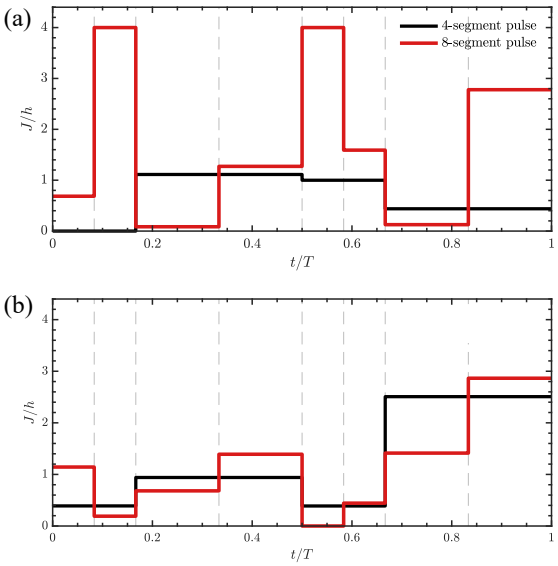


Fig. 3. Comparison of the optimized four-segment and eight-segment exchange pulses to implement the (a) CZ and (b) CNOT gate. The eight-segment pulse is obtained by dividing each BB1 time segment into two equal subsegments while keeping the total gate time unchanged, thereby providing additional degrees of freedom in the exchange control. The black and red curves denote the four-segment and eight-segment exchange pulses, respectively.

6. Iterate the propagation, fidelity evaluation, and control update until the cost function converges. To avoid local optima, several initial guesses for **J** are tested, and the solution with the highest robust fidelity is selected.

One optimized solution is

$$J_{\mathrm{CZ}}^{(4)}(t)/h=\begin{cases}0, & 0\le t<t_1,\\ 1.11245494, & t_1\le t<t_2,\\ 0.99916315, & t_2\le t<t_3,\\ 0.43833708, & t_3\le t<T\end{cases}. \tag{29}$$

Here, $t_1=\tau_1$, $t_2=\tau_1+\tau_2$, $t_3=\tau_1+\tau_2+\tau_3$ and $T=\tau_1+\tau_2+\tau_3+\tau_4$. The pulse shape of $J(t)$ is shown in Fig. 3(a) by the black line. Substituting these four values into Eq. (21) yields the desired $Z(\pi)$ operation in the S_2 block, up to an irrelevant phase, which can be compensated by appropriately choosing ΔE_z and ΔE_z^1 [37].

As shown in Figs. 4(a) and (c), although this pulse (black lines) can give a high fidelity at the zero-error point, its robustness is limited because only four independent exchange amplitudes are available. The fidelity is sensitive to both the microwave amplitude error ϵ_h and the exchange amplitude error ϵ_J, indicating that the four-segment pulse does not provide enough control freedom to suppress the two error channels simultaneously. We therefore further divide each BB1 segment into two equal subsegments, while keeping the

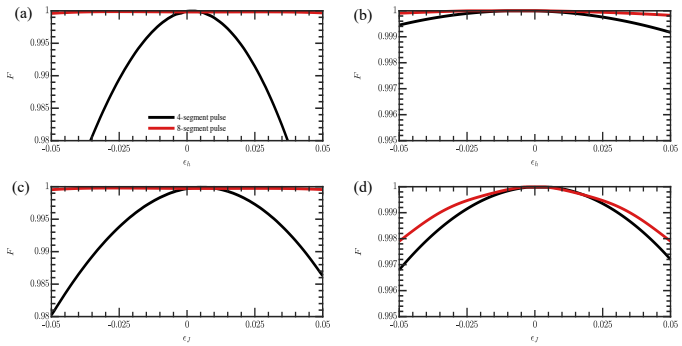


Fig. 4. Robustness of the optimized exchange pulses for the CZ and CNOT gates. Panels (a) and (c) show the fidelity of the CZ gate as a function of the error ϵ_h and ϵ_J, respectively. Panels (b) and (d) show the corresponding results for the CNOT gate. The black and red curves denote the four-segment and eight-segment exchange pulses, respectively.

total duration of every BB1 segment unchanged. This leads to an eight-segment exchange pulse with eight independently optimized amplitudes as

$$J_{\mathrm{CZ}}^{(8)}(t)/h=\begin{cases}0.65585339 & 0\le t<\frac{t_1}{2},\\ 4.00000000 & \frac{t_1}{2}\le t<t_1,\\ 0.12514711 & t_1\le t<\frac{t_1+t_2}{2},\\ 1.29087007 & \frac{t_1+t_2}{2}\le t<t_2,\\ 4.00000000 & t_2\le t<\frac{t_2+t_3}{2},\\ 1.55349573 & \frac{t_2+t_3}{2}\le t<t_3,\\ 0.15156974 & t_3\le t<\frac{t_3+T}{2},\\ 2.79557362 & \frac{t_3+T}{2}\le t<T.\end{cases} \tag{30}$$

The increased number of control parameters allows the S_2 evolution to better compensate for the simultaneous fluctuations in h and J. As a result, the optimized eight-segment pulse shows a much flatter fidelity profile over the same error range. In the two-qubit simulation, we use the fidelity defined as

$$F_{\mathrm{avg}}=\frac{\left|\mathrm{Tr}\left(U_{\mathrm{tar}}^{\dagger}U_{\epsilon}\right)\right|^2+d}{d(d+1)} \tag{31}$$

where d denotes the dimension of the matrix, and we take $d=4$ in this work. U_{tar} and U_{ϵ} denote the target unitary and noisy evolution operator, respectively. In addition, for both types of errors in the experimentally relevant range of $[-0.05, 0.05]$ [13], the fidelity of the eight-segment pulse remains above 99.9%, as shown for the red lines in Figs. 4(a) and (c). This comparison demonstrates that the additional subdivision of the exchange pulse is essential for achieving robust two-qubit gate operation.

We then simulate the optimized CZ gate under quasistatic Gaussian noise. In each realization, the

microwave amplitude error ϵ_h and the exchange amplitude error ϵ_J are sampled independently from normal distributions, $\epsilon_h \sim \mathcal{N}(0, \sigma_h^2)$ and $\epsilon_J \sim \mathcal{N}(0, \sigma_J^2)$, where σ_h and σ_J denote the corresponding standard deviations. The fidelity is averaged over 5000 noise realizations. As shown in Figs. 5(a) and (c), the eight-segment pulse (red lines) gives a lower infidelity than the four-segment pulse (black lines) over a broad range of noise strengths. For the experimentally relevant values $\sigma_h \sim 0.0016$ and $\sigma_J \sim 0.0097$ [13], the optimized CZ gate reaches $F = 99.9458\%$ for the four-segment pulse and $F = 99.9897\%$ for the eight-segment pulse, demonstrating the robustness of the proposed pulse design against realistic quasistatic control fluctuations.

3.3. CNOT gate

To implement a CNOT gate, the duration of each segment fixed by the BB1 pulse is

$$\tau_1 = \tau_3 = \frac{\pi}{h}, \quad \tau_2 = \frac{2\pi}{h}, \quad \tau_4 = \frac{\pi}{h}. \tag{32}$$

After the BB1 construction in the S_1 block, these four pulse durations $\{\tau_k\}_{k=1}^4$ are fixed. Similar to the CZ gate above, these durations must be used simultaneously in the S_2 block. Using the same algorithm as described above, we obtain the four-segment pulse as

$$J_{\mathrm{CNOT}}^{(4)}(t)/h = \begin{cases} 0.38952892, & 0 \le t < t_1, \\ 0.94073504, & t_1 \le t < t_2, \\ 0.38826091, & t_2 \le t < t_3, \\ 2.50720288, & t_3 \le t < T, \end{cases} \tag{33}$$

and the eight-segment pulse as

$$J_{\mathrm{CNOT}}^{(8)}(t)/h = \begin{cases} 1.14295895, & 0 \le t < \frac{t_1}{2}, \\ 0.19034721, & \frac{t_1}{2} \le t < t_1, \\ 0.68154049, & t_1 \le t < \frac{t_1+t_2}{2}, \\ 1.39102114, & \frac{t_1+t_2}{2} \le t < t_2, \\ 0.00000000, & t_2 \le t < \frac{t_2+t_3}{2}, \\ 0.44329663, & \frac{t_2+t_3}{2} \le t < t_3, \\ 1.41326038, & t_3 \le t < \frac{t_3+T}{2}, \\ 2.86454421, & \frac{t_3+T}{2} \le t < T \end{cases}. \tag{34}$$

The corresponding pulse shapes are shown in Figs. 3(b).

Figs. 4(b) and (d) compare the two-qubit CNOT gate fidelity obtained with the optimized four-segment and eight-segment exchange pulses. Compared with the CZ gate, the four-segment pulse already gives relatively good robustness for the CNOT gate, because the relevant NOT operation in the S_1 subspace is protected by the BB1 sequence with a shorter evolution time and the corresponding S_2 operation is optimized as an identity operation. However, the eight-segment pulse still produces a flatter fidelity profile under both ϵ_h and ϵ_J. The improvement is particularly evident for exchange amplitude errors, where the four-segment pulse shows a stronger fidelity reduction near the edge of the error window. This comparison indicates that the eight-segment construction is not only essential for the robust CZ gate but also further enhances the robustness of the CNOT gate.

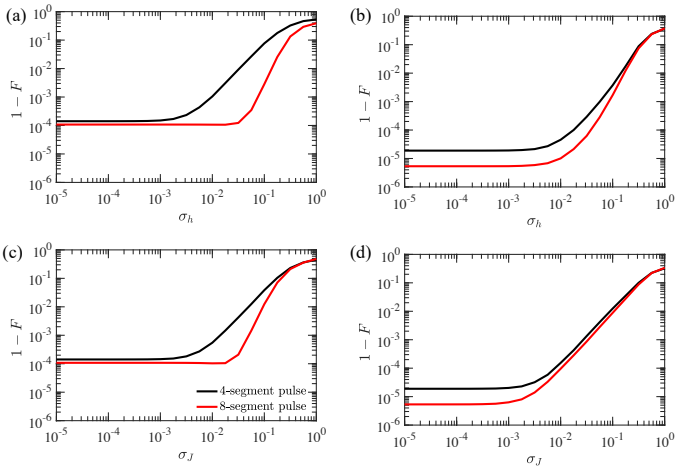


Fig. 5. Infidelity of the optimized CZ and CNOT gates under quasistatic Gaussian noise. Panels (a) and (c) correspond to the CZ gate, and panels (b) and (d) correspond to the CNOT gate. The black and red curves denote the four-segment and eight-segment exchange pulses, respectively.

Figs. 5(b) and (d) show the CNOT gate infidelity under quasistatic Gaussian noise. Compared with the CZ gate, the CNOT gate exhibits a lower infidelity when the noise is small, mainly because the S_2 target operation is the identity rather than a $Z(\pi)$ rotation. The eight-segment pulse still improves the robustness over the four-segment pulse by providing additional exchange control degrees of freedom. For the experimentally relevant noise strengths, the fidelity increases from $F = 0.999856$ for the four-segment pulse to $F = 0.999911$ for the eight-segment pulse, demonstrating the robustness of the optimized CNOT gate against realistic microwave amplitude and exchange amplitude fluctuations.

4. Conclusions

In conclusion, we have proposed a hybrid composite pulse and numerical optimization protocol for robust two-qubit gates in silicon double quantum dots. By transforming the driven two-spin Hamiltonian into the rotating frame, the system is approxi-

mately decomposed into two effective subspaces. The microwave-dominated S_1 subspace is protected by the BB1 composite pulse, while the exchange-assisted S_2 subspace is optimized using a GRAPE-like search over piecewise exchange amplitudes. Using this framework, we construct both CZ and CNOT gates and compare four-segment and eight-segment exchange pulses. The results show that the eight-segment pulse provides additional control freedom and significantly improves the robustness against both microwave amplitude and exchange amplitude errors. Under experimentally relevant quasistatic Gaussian noise, the optimized CZ and CNOT gates reach fidelities of 99.9897% and 99.9911%, respectively. For experimental implementation, the piecewise-constant $J(t)$ should be regarded as an ideal target waveform, since finite control-line bandwidth and imperfect transmission may smooth or distort the applied pulse. Finite rise and fall times can be incorporated by replacing the abrupt transitions with a smooth continuous waveform, while transmission-induced distortions can be compensated using experimentally calibrated predistortion techniques [14,38]. These results demonstrate that the proposed protocol offers a practical and experimentally compatible route to robust two-qubit gates in silicon.

Acknowledgments

This work was supported by the Guangxi Bagui Young Talents Program, the Shenzhen International Quantum Academy (Grant No. SIQA2025KFKT08), and the National Key Research and Development Program of China (2025YFE0217900).

References

[1] Loss D and DiVincenzo D P 1998 *Phys. Rev. A* **57** 120
[2] Kane B E 1998 *Nature* **393** 133
[3] Hanson R, Kouwenhoven L P, Petta J R, Tarucha S and Vandersypen L M K 2007 *Rev. Mod. Phys.* **79** 1217
[4] Zwanenburg F A, Dzurak A S, Morello A, Simmons M Y, Hollenberg L C L, Klimeck G, Rogge S, Coppersmith S N and Eriksson M A 2013 *Rev. Mod. Phys.* **85** 961
[5] Veldhorst M, Eenink H G J, Yang C H and Dzurak A S 2017 *Nat. Commun.* **8** 1766
[6] Veldhorst M, Yang C H, Hwang J C C, Huang W, Dehollain J P, Muhonen J T, Simmons S, Laucht A, Hudson F E, Itoh K M, Morello A and Dzurak A S 2015 *Nature* **526** 410
[7] Zajac D M, Sigillito A J, Russ M, Borjans F, Taylor J M, Burkard G and Petta J R 2018 *Science* **359** 439
[8] Watson T F, Philips S G J, Kawakami E, Ward D R, Scarlino P, Veldhorst M, Savage D E, Lagally M G, Friesen M, Coppersmith S N, Eriksson M A and Vandersypen L M K 2018 *Nature* **555** 633
[9] Xue X, Watson T F, Helsen J, Ward D R, Savage D E, Lagally M G, Coppersmith S N, Eriksson M A, Wehner S and Vandersypen L M K 2019 *Phys. Rev. X* **9** 021011
[10] Huang W, Yang C H, Chan K W, Tanttu T, Hensen B, Leon R C C, Fogarty M A, Hwang J C C, Hudson F E, Itoh K M, Morello A and Dzurak A S 2019 *Nature* **569** 532
[11] Philips S G J, Madzik M T, Amitonov S V, de Snoo S L, Russ M, Kalhor N, Volk C, Lawrie W I L, Brousse D, Tryputen L, Sammak A, Veldhorst M, Scappucci G and Vandersypen L M K 2022 *Nature* **609** 919
[12] Noiri A, Takeda K, Nakajima T, Kobayashi T, Sammak A, Scappucci G and Tarucha S 2022 *Nature* **601** 338
[13] Xue X, Russ M, Samkharadze N, Undseth B, Sammak A, Scappucci G and Vandersypen L M K 2022 *Nature* **601** 343
[14] Mills A R, Guinn C R, Gullans M J, Sigillito A J, Feldman M M, Nielsen E and Petta J R 2022 *Sci. Adv.* **8** eabn5130
[15] Jiang S-L, Jiang T-Y, Xu Y-Q, Wu R, Hao T-Y, Ye S-K, Cai R-R, Wang B-C, Li H-O, Cao G and Guo G-P 2024 *Chin. Phys. B* **33** 090311
[16] Ma R-L, Ni M, Zhou Y-C, Kong Z-Z, Wang G-L, Liu D, Luo G, Cao G, Li H-O and Guo G-P 2024 *Chin. Phys. B* **33** 060312
[17] Huang J Y, Su R Y, Lim W H, Feng M, van Straaten B, Severin B, Gilbert W, Dumoulin Stuyck N, Tanttu T, Serrano S, Cifuentes J D, Hansen I, Seedhouse A E and Vahapoglu E 2024 *Nature* **627** 772
[18] Tanttu T, Lim W H, Huang J Y, Dumoulin Stuyck N, Gilbert W, Su R Y, Feng M, Cifuentes J D and Seedhouse A E 2024 *Nat. Phys.* **20** 1804
[19] Steinacker P, Dumoulin Stuyck N, Lim W H, Tanttu T, Feng M and Serrano S 2025 *Nature* **646** 81
[20] Thorvaldson I, Poulos D, Moehle C M, Misha S H, Edlbauer H, Reiner J, Geng H, Voisin B, Jones M T and Donnelly M B 2025 *Nat. Nanotechnol.* **20** 472
[21] Wu Y H, Camenzind L C, Butler P, Jin I K, Noiri A, Takeda K, Nakajima T, Kobayashi T, Scappucci G, Goan H S and Tarucha S 2025 (arXiv.2507.11918)
[22] Edlbauer H, Wang J, Huq A M S E, Thorvaldson I, Jones M T, Misha S H, Pappas W J, Moehle C M, Hsueh Y L, Bornemann H, Gorman S K, Chung Y, Keizer J G, Kranz L and Simmons M Y 2025 *Nature* **648** 569
[23] Dial O E, Shulman M D, Harvey S P, Bluhm H, Umansky V and Yacoby A 2013 *Phys. Rev. Lett.* **110** 146804
[24] Connors E J, Nelson J, Edge L F and Nichol J M 2022 *Nat. Commun.* **13** 940
[25] Rimbach-Russ M, Philips S G J, Xue X and Vandersypen L M K 2023 *Quantum Sci. Technol.* **8** 045025
[26] Levitt M H 1986 *Prog. Nucl. Magn. Reson. Spectrosc.* **18** 61
[27] Wimperis S 1994 *J. Magn. Reson. Ser. A* **109** 221
[28] Cummins H K and Jones J A 2000 *New J. Phys.* **2** 6
[29] Brown K R, Harrow A W and Chuang I L 2004 *Phys. Rev. A* **70** 052318
[30] Khaneja N, Reiss T, Kehlet C, Schulte-Herbrüggen T and Glaser S J 2005 *J. Magn. Reson.* **172** 296
[31] Glaser S J, Boscain U, Calarco T, Koch C P, Köckenberger W, Kosloff R, Kuprov I, Luy B, Schirmer S, Schulte-Herbrüggen T, Sugny D and Wilhelm F K 2015 *Eur. Phys. J. D* **69** 279
[32] Koch C P, Boscain U, Calarco T, Dirr G, Filipp S, Glaser S J, Kosloff R, Montangero S, Schulte-Herbrüggen T, Sugny D and Wilhelm F K 2022 *EPJ Quantum Technol.* **9** 19
[33] Rossignolo M, Reisser T, Marshall A, Rembold P, Pagano A, Vetter P J, Said R S, Mueller M M, Motzoi F, Calarco T, Jelezko F and Montangero S 2023 *Comput. Phys. Commun.* **291** 108782
[34] Russ M, Zajac D M, Sigillito A J, Borjans F, Taylor J M, Petta J R and Burkard G 2018 *Phys. Rev. B* **97** 085421
[35] Calderon-Vargas F A, Barron G S, Deng X H, Sigillito A J, Barnes E and Economou S E 2019 *Phys. Rev. B* **100** 035304
[36] Wang X, Bishop L S, Barnes E, Kestner J and Das Sarma S 2014 *Phys. Rev. A* **89** 022310
[37] Lu Y Y, Wei K and Zhang C 2025 *Phys. Rev. A* **111** 042609
[38] Ni M, Ma R-L, Kong Z-Z, Chu N, Liao W-Z, Zhu S-K, Wang C, Luo G, Liu D, Cao G, Wang G-L, Li H-O and Guo G-P 2025 *Chin. Phys. B* **34** 010308